

10.24425/acs.2023145120

Archives of Control Sciences
Volume 33(LIX), 2023
No. 1, pages 239–271

Probing 3D chaotic Thomas' cyclically attractor with multimedia encryption and electronic circuitry

NajeebAlam KHAN, Muhammad Ali QURESHI, Saeed AKBAR and Asmat ARA

This study investigates Thomas' cyclically symmetric attractor dynamics with mathematical and electronic simulations using a proportional fractional derivative to comprehend the dynamics of a given chaotic system. The three-dimensional chaotic flow was examined in detail with Riemann-Liouville derivative for different values of the fractional index to highlight the sensitivity of chaotic systems with initial conditions. Thus, the dynamics of the fractional index system were investigated with Eigenvalues, Kaplan–Yorke dimension, Lyapunov exponent, and NIST testing, and their corresponding trajectories were visualized with phase portraits, 2D density plot, and Poincaré maps. After obtaining the results, we found that the integer index dynamics are more complex than the fractional index dynamics. Furthermore, the chaotic system circuit is simulated with operational amplifiers for different fractional indices to generate analog signals of the symmetric attractor, making it an important aspect of engineering. The qualitative application of our nonlinear chaotic system is then applied to encrypt different data types such as voice, image, and video, to ensure that the developed nonlinear chaotic system can widely applied in the field of cyber security.

Key words: Thomas' cyclically attractor, fractional calculus, chaos, encryption

1. Introduction

The deterministic, irregular, and unpredictable behavior of dynamical systems has gained a lot of attention in recent years. With fast-evolving applications in the fields of multimedia, digital networks, cyber security, and information sciences, irregular-deterministic behavior has gained considerable attention. Deterministic-nonlinear dynamical systems, widely known as chaos, have now been considered as an interdisciplinary subject with applications in the fields of physics [1, 2], biology [3], economics [4], medicine [5], communication [6], cryptography [7],

Copyright © 2023. The Author(s). This is an open-access article distributed under the terms of the Creative Commons Attribution-NonCommercial-NoDerivatives License (CC BY-NC-ND 4.0 <https://creativecommons.org/licenses/by-nc-nd/4.0/>), which permits use, distribution, and reproduction in any medium, provided that the article is properly cited, the use is non-commercial, and no modifications or adaptations are made

NA. Khan (corresponding author, e-mail: njbalam@yahoo.com) and S. Akbar are with Department of Mathematics, University of Karachi, Karachi 75270, Pakistan.

M.A. Qureshi is with Department of Physics, University of Karachi, Karachi 75270, Pakistan.

A. Ara is with College of Humanities and Sciences, PAF-KIET, Karachi 75190, Pakistan.

Received 28.09.2022. Revised 27.01.2023.

electronics [8,9] etc. The evolution of chaos after Lorenz [10], a two-scroll chaotic attractor led to the development of one scroll attractor [11], three scroll attractor [12], six scroll attractor [13], and multi-scroll attractor [14]. The attractors were studied and researched in detail, such as limit cycle attractors presented by Vanderpole [15] in his study of force triod vibration, a model of electronic circuits that was used in radio. Subsequently, attractors like Rossler were explored under the time-scale perspective by Dimitris et.al. [16]. Chua's attractor hidden bifurcations novel methodology was introduced to study the multispiral Chua attractor completely [17]. Additional ideas and methodologies are under investigation in nonlinear dynamical systems to probe the natural phenomena present in this world. Other renowned attractors include Chen attractor [18], Lu Chen attractor [19], PWL duffing chaotic attractor [20], Rabinovich-Fabrikant attractor [21], etc.

Fractional derivatives, with enormous influence on the history of non-integer order systems in the field of science and technology, have greatly affected the development of chaotic systems [22,23]. As a generalization of classical derivatives, fractional derivatives are used to describe and solve ordinary and partial differential equations along with integral equations. With well-known definitions of fractional derivatives, such as Liouville, Riezs, Riemann, Atangana–Baleanu, Caputo, Letnikov, Hadamard, Marchaud, Weyl, and Coimbra, fractional derivatives have enormous interdisciplinary applications. The current contributions of fractional derivatives in the field of fractional index chaotic systems are numerous, such as the effects of the modified Chua's system studied by Tom et al. with fractional derivatives [24]. Recently, chaos dynamics control has gained popularity, with a new trend of investigating chaotic systems using different mathematical and physical models, such as Chunguang and Guanrong, who studied the Chen system with fractional order [25]. Digital/analog electronics and fractional index systems play a significant role in the investigation of chaotic regimes and in the design of low-power consumption systems with quick processing units. Digital systems and their component perspectives, such as adaptive controllers with implementation to FPGA, are presented for fractional index in a cubic nonlinear resistor system [26]. Moaddy et al. investigated the Rabinovich-Fabrikant model under the Caputo fractional derivative with its simulation on a multistep generalized differential transform (MsGDT) [27]. In Hopfield-type neural networks, fractional-order dynamics were investigated [28].

Chaotic systems with deterministic random-number generation are important in electronics and cryptography. The sensitivity of the system to the initial conditions allows this random number generation to be another remarkable feature of data encryption. Sophisticated algorithms and fractional-orders are added to the system roots to produce a rock-solid security feature that is now a core part of our daily life in data handling. Cryptography has advanced significantly, with data scrambling application in voice, GIF, image, and PDF with XOR operation

to secure the data in *PYTHON* programming performed by Khan et al. [29, 30]. Harinato et al. utilized advanced encryption systems (AES) and steganography for security and data exchange [31]. Further, complicated systems and encryption processes are designed to protect user data from third parties. As data science evolves, new methods and approaches have been developed to ensure global communication.

In this work, we investigate numerical analysis, electronic simulation, and multimedia (voice, image, and video) encryption using Riemann-Liouville fractional derivative of Thomas' cyclically symmetric attractor. The dynamical behavior of Thomas' cyclically symmetric attractors was analyzed and investigated with respect to different fractional indexes. The electronic circuits were designed using *MultiSim* software, and the circuit realization was simulated with voltage operational amplifiers, multipliers, resistors, and capacitors. Image encryption is carried out in *PYTHON* using a bit-wise exclusive OR operator with two keys: (1) the chaotic system and (2) the plain image. Both keys are important for decoding the images and videos. The image is processed and analyzed with unified average changing intensity, peak signal-to-noise ratio, root mean square error, number of pixels change rate, and correlation coefficients between the pixel data to ensure a security system with better protection against hackers.

2. Thomas cyclically chaotic model

Here, we consider the chaotic system which has been proposed by Thomas [32]. His work consisted of a three dimensional system of differential equations which is as follows:

$$\begin{aligned}
 x_1(t) &= -gx_1(t) + hx_2(t) - (x_2(t))^3, \\
 x_2(t) &= -gx_2(t) + hx_3(t) - (x_3(t))^3. \\
 x_3(t) &= -gx_3(t) + hx_1(t) - (x_1(t))^3
 \end{aligned} \tag{1}$$

where, $x_1(t)$, $x_2(t)$ and $x_3(t)$ are dependent variables, g and h are constant parameters with the values $g = 0.3$ and $h = 1.1$. The initial conditions used for numerical and graphical solutions are $(x_1(0), x_2(0), x_3(0)) = (1, 0, 1)$.

Definition 1 *The Riemann-Liouville operator, which is one of the most popular fractional integral operators of an order α of a real function $\chi(y) \in C_\mu$, $\mu \geq -1$ is given by:*

$$D^\alpha \chi(y) = \frac{1}{\Gamma(\alpha)} \int_0^y (y-t)^{\alpha-1} \chi(t) dt, \tag{2}$$

$\alpha > 0$, $\chi > 0$ and $D^0 \chi(y) = \chi(y)$.

The operator D^α has some properties, for $\alpha, \alpha_1 \geq 0$ and $\alpha_3 \geq -1$.

$$\begin{aligned} D^\alpha D^{\alpha_1} \chi(y) &= D^{\alpha+\alpha_1} \chi(y), \\ D^\alpha D^{\alpha_1} \chi(y) &= D^{\alpha_1} D^\alpha \chi(y), \\ D^\alpha y^{\alpha_3} &= \frac{\Gamma(\alpha_3 + 1)}{\Gamma(\alpha + \alpha_3 + 1)} y^{\alpha+\alpha_3}. \end{aligned}$$

The Laplace transform of R-L Integral/Derivative is

$$L \{D_0^p f(x), s\} = s^p F(s) - \sum_{k=0}^{n-1} s^k \left[D_0^{p-k-1} f(0) \right]. \quad (3)$$

Thus while solving fractional differential equations involving RL derivative, initial conditions of the form $D_0^{p-k-1} f(0)$ are required which have no physical interpretation. This limitation of RL derivative, is overcome by Caputo derivative introduced by Caputo.

Definition 2 The Caputo fractional derivative D^q of the function $g(x)$ of order q such that $n - 1 < q \leq n$, $n \in \mathbb{N}$, for $t > 0$ and $g \in C_{-1}^n$ in the expression of E^q is:

$$D^q g(x) = E^{n-q} D^n g(x) = \frac{1}{\Gamma(n-q)} \int_0^x (x-t)^{n-q-1} g^{(n)}(t) dt \quad (4)$$

and has the following properties for $n - 1 < q \leq n$, $n \in \mathbb{N}$, $\mu \geq -1$ and $g \in C_\mu^n$:

$$\begin{aligned} D^q E^q g(x) &= g(x), \\ E^q D^q g(x) &= g(x) - \sum_{k=0}^{n-1} g^{(k)}(0^+) \frac{x^k}{k!} \end{aligned}$$

for $x > 0$.

The relationship between RL and Caputo is defined by

$${}^{RL}D_a^q f(x) = {}^C D_a^q f(x) + \sum_{k=0}^{n-1} \frac{f^{(k)}(a)(x-a)^{k-q}}{\Gamma(k-q+1)}. \quad (5)$$

Thus, the two definitions RL ${}^{RL}D_a^q$ and Caputo ${}^C D_a^q$ will be equivalent iff, $f^{(k)}(a) = 0$, $0 \leq k \leq n - 1$.

Definition 3 *The Oustaloup recursive approximation (ORA) allows approximating an elementary FO transfer function s^α by the finite, integer-order transfer function, close to Pade approximation is:*

$$s^\alpha = k_f \prod_{n=1}^N \left(\frac{1 + \frac{s}{\mu_n}}{1 + \frac{s}{\nu_n}} \right) = \frac{L_\alpha(s)}{M_\alpha(s)}. \quad (6)$$

In the above equation, N is the order of the approximation, k_f is the steady state gain, μ_n and ν_n are calculated as follows:

$$\begin{aligned} \mu_1 &= \omega_l \sqrt{N}, \\ \nu_n &= \mu_n \gamma, \quad n = 1, \dots, N \\ \mu_{n+1} &= \nu_n \eta, \quad n = 1, \dots, N - 1, \end{aligned} \quad (7)$$

where,

$$\begin{aligned} \gamma &= \left(\frac{\omega_h}{\omega_l} \right)^{\frac{\alpha}{N}}, \\ \eta &= \left(\frac{\omega_h}{\omega_l} \right)^{\frac{1-\alpha}{N}}. \end{aligned} \quad (8)$$

In equation (7), ω_l and ω_h describe the range of angular frequency, for which parameters should be calculated. A steady state gain k_f is set to assure convergence of the approximation to the real plant's step response.

3. Fractional order chaotic system and numerical simulations

In this section the fractional order chaotic system is presented along with its numerical simulation, the model is given as

$$\begin{aligned} D^q x_1(t) &= -g x_1(t) + h x_2(t) - (x_2(t))^3, \\ D^q x_2(t) &= -g x_2(t) + h x_3(t) - (x_3(t))^3, \\ D^q x_3(t) &= -g x_3(t) + h x_1(t) - (x_1(t))^3, \end{aligned} \quad (9)$$

where $x_1(t)$, $x_2(t)$ and $x_3(t)$ are dependent variables, D^q is a fractional-order derivative with index q and, g , h are constant parameters with the values $g = 0.3$ and $h = 1.1$. The initial conditions used for numerical and graphical solutions are $(x_1(0), x_2(0), x_3(0)) = (1, 0, 1)$.

To investigate the proposed systems, equation (1) and (9) was solved numerically. Initially, the time series plot is generated for the fractional index chaotic differential equation system for $x_1(t)$, $x_2(t)$ and $x_3(t)$. Figure 1 shows the fractional order $q = 1$, in which we can see that the signal oscillates non-periodically on positive amplitudes of the graph, and after some time interval Δt , it begins to oscillate downward with negative amplitudes, and so forth. Figures 2 and 3 shows the fractional order $q = 0.99$, and $q = 0.95$ where we can see that the nonlinearity remains the same throughout the elapsed time. The $x_1(t)$, $x_2(t)$ and $x_3(t)$ are then plotted in 2D phase portraits in the combinations of $(x_1(t), x_2(t))$, $(x_1(t), x_3(t))$ and $(x_2(t), x_3(t))$ in Figs. 4, 5 and 6 respectively for different values of q . Subsequently, the 3D plots are generated in Fig. 7a–c to visualize the chaotic attractors and their dimensions magnitude $x_1(t)$, $x_2(t)$ and $x_3(t)$ together. The Poincare plots are plotted in Fig. 8a–f for fractional index $q = 1$ and $q = 0.99$ to represent the chaotic trajectory flow calculated in each cycle of motion. The 2D

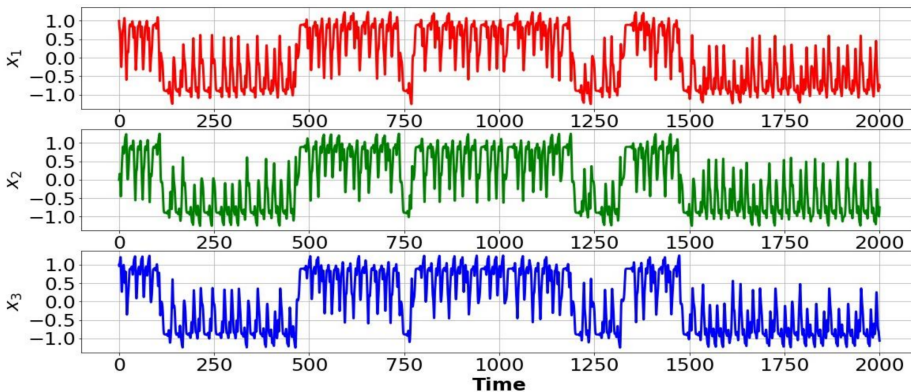


Figure 1: Time series plots of $x_1(t)x_2(t)x_3(t)$ at fractional order $q = 1$

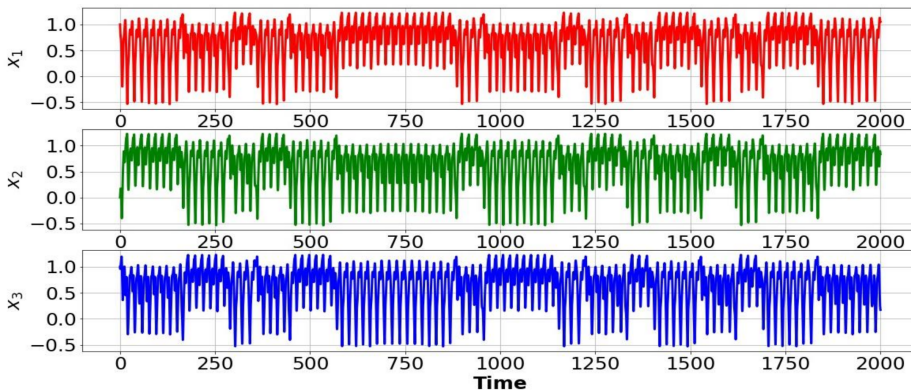


Figure 2: Time series plots of $x_1(t)x_2(t)x_3(t)$ at fractional order $q = 0.99$

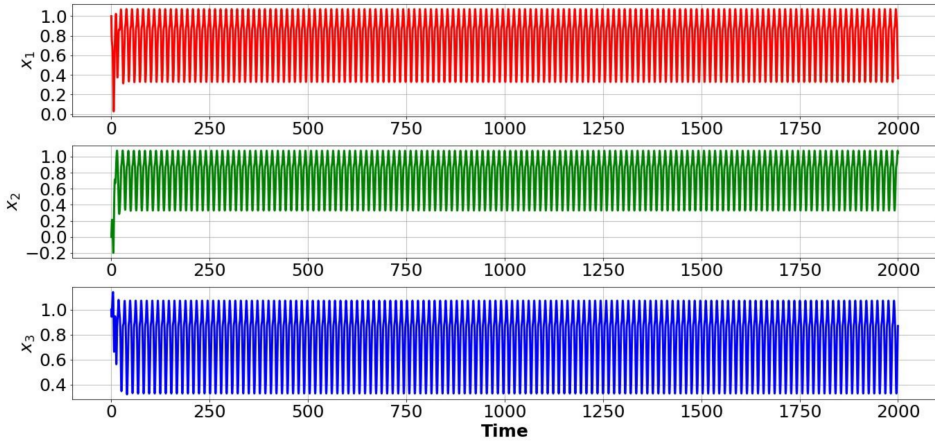
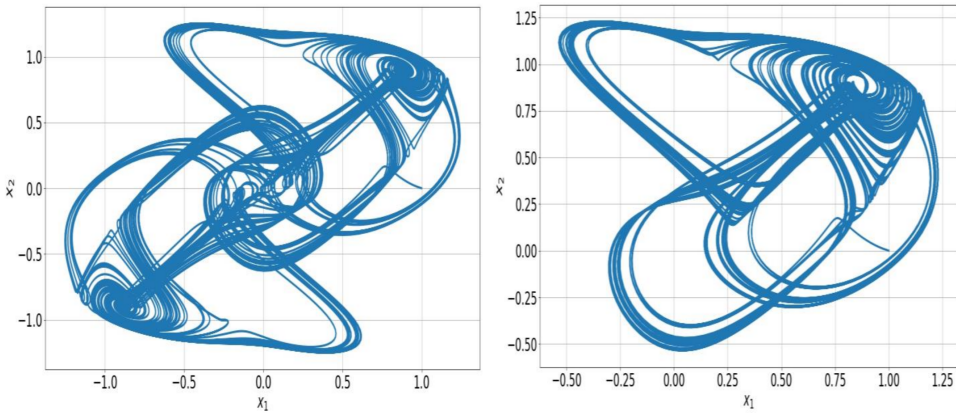
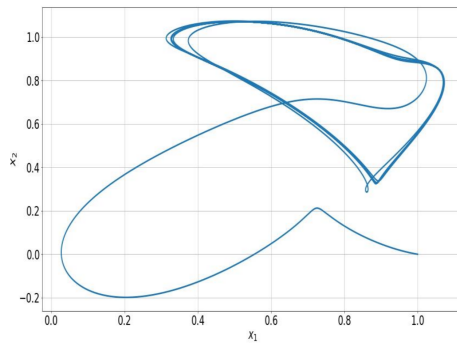


Figure 3: Time series plots of $x_3(t)$ at fractional order $q = 0.95$



(a) $q = 1$

(b) $q = 0.99$



(c) $q = 0.95$

Figure 4: 2D plots of $(x_1(t), x_2(t))$ at different values of fractional-order q

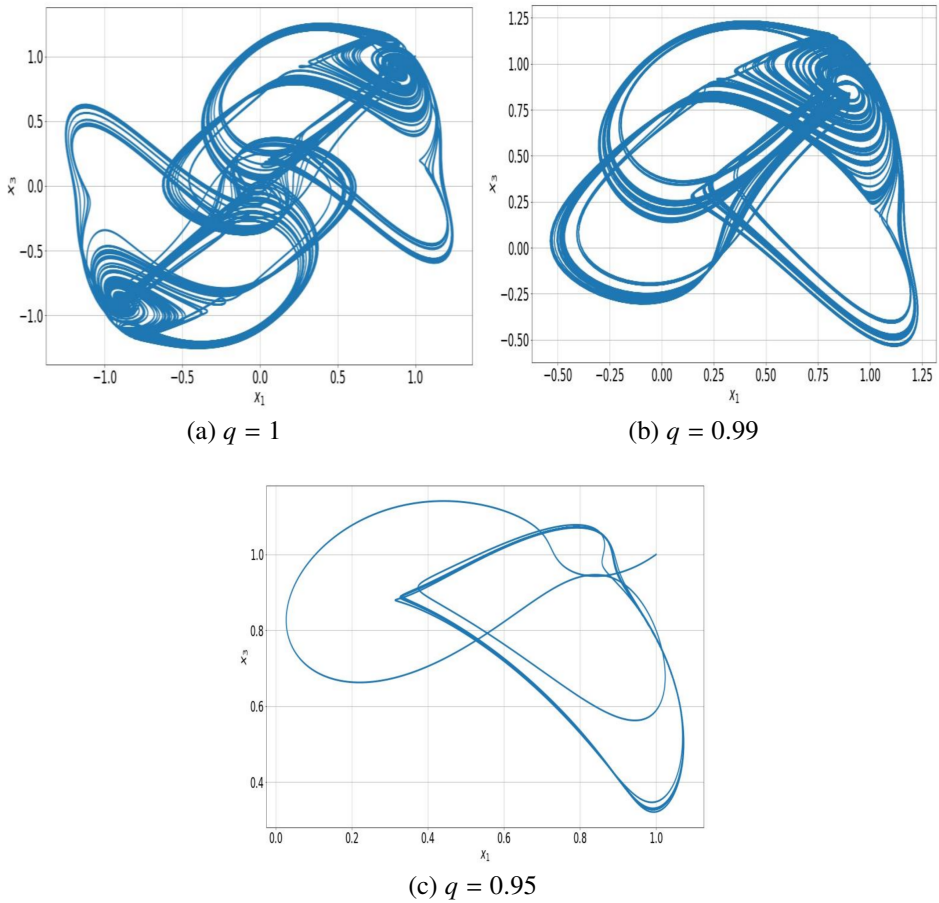
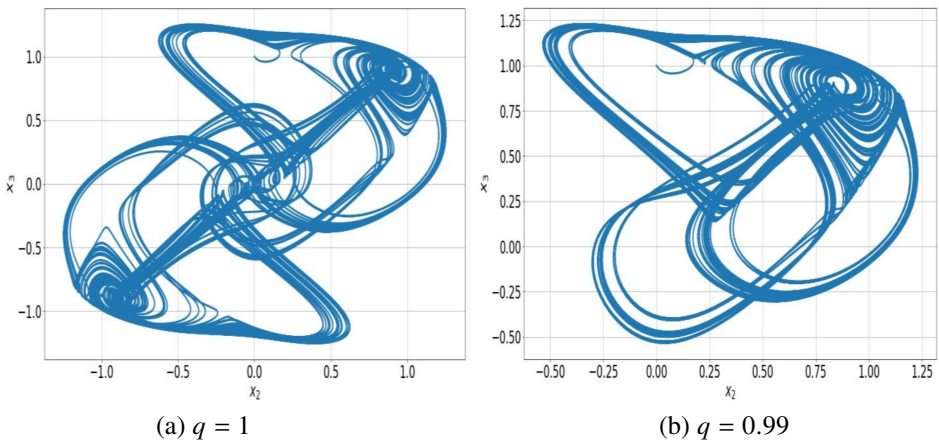
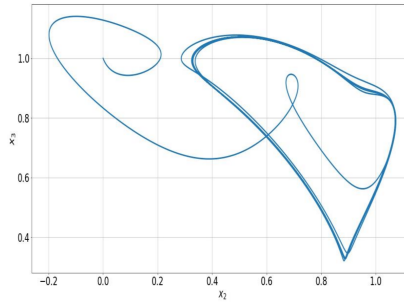
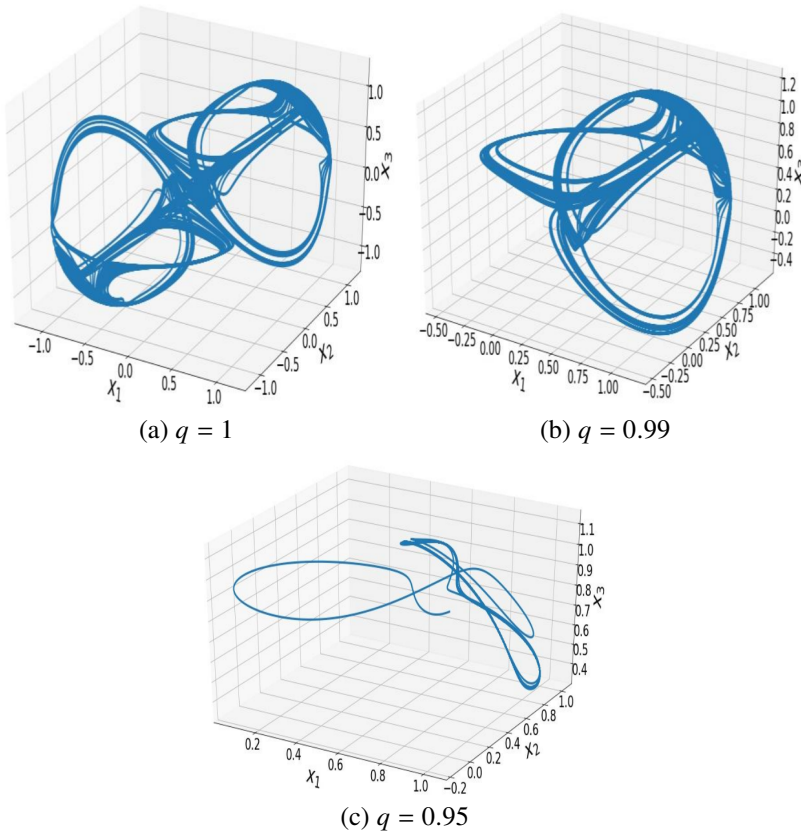


Figure 5: 2D plots of $(x_1(t), x_3(t))$ at different values of fractional-order q



(c) $q = 0.95$ Figure 6: 2D plots of $(x_2(t), x_3(t))$ at different values of fractional-order q Figure 7: 3D plots of $(x_1(t), x_2(t))$ at different values of fractional-order q

contour plots for $q = 1$ and $q = 0.99$ are illustrated in Fig. 9a–f for $(x_1(t), x_2(t))$, $(x_1(t), x_3(t))$, $(x_2(t), x_3(t))$ -planes respectively, and the advantage of this plot is that the probability of attractor is mostly generated at the point where the contours are dense and is in good agreement with our plotted phase portraits.

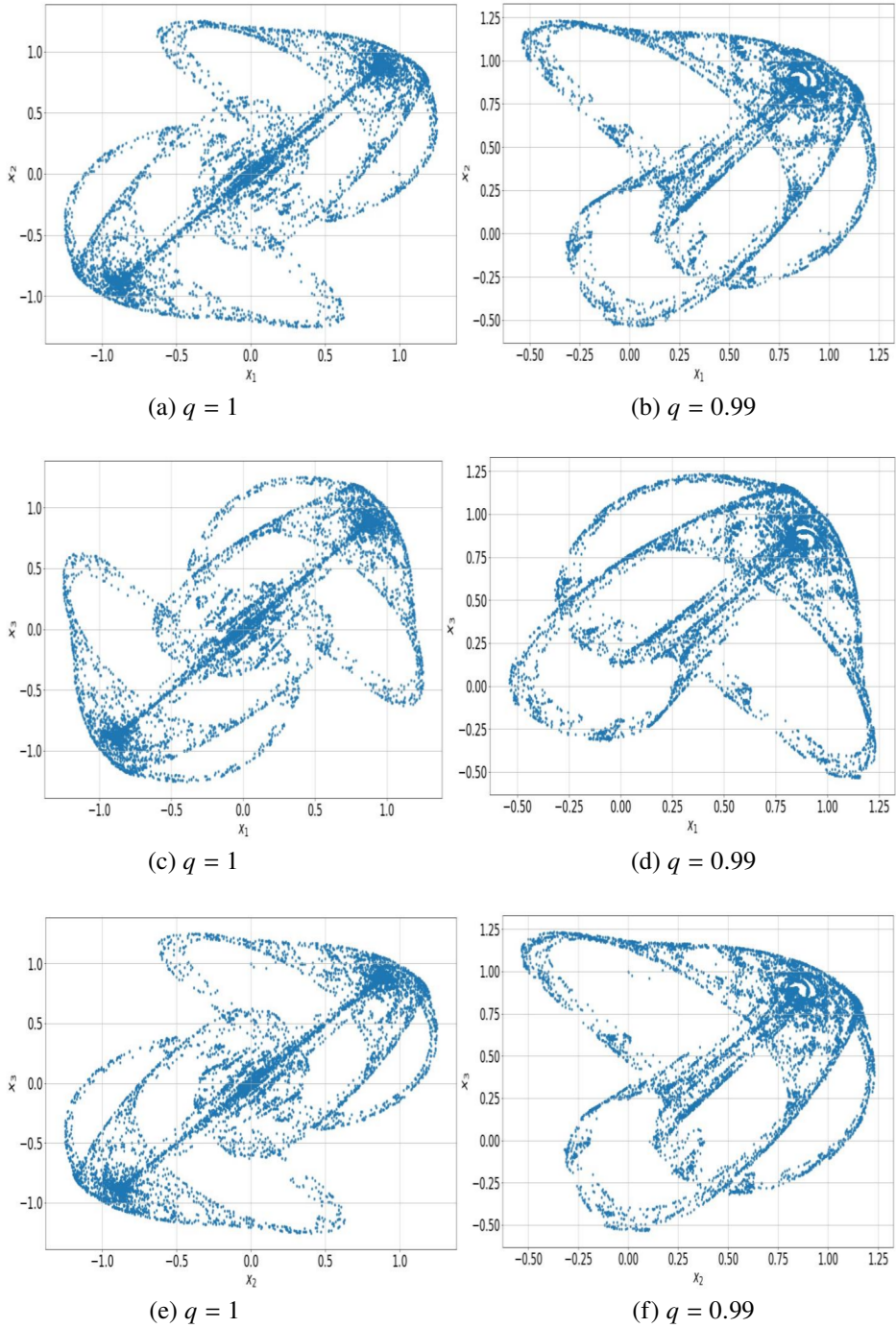
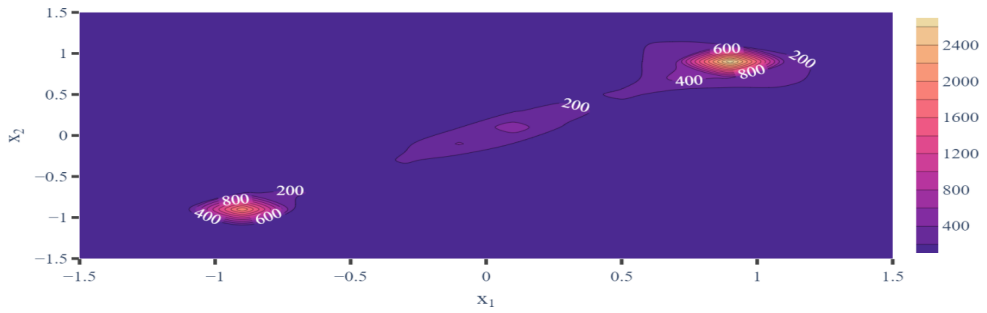
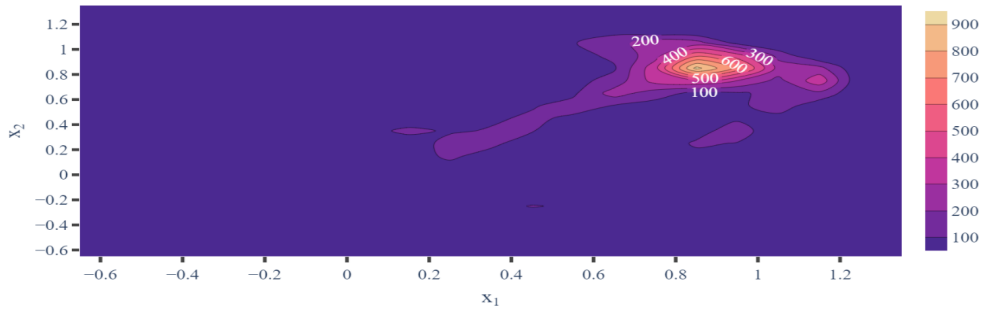


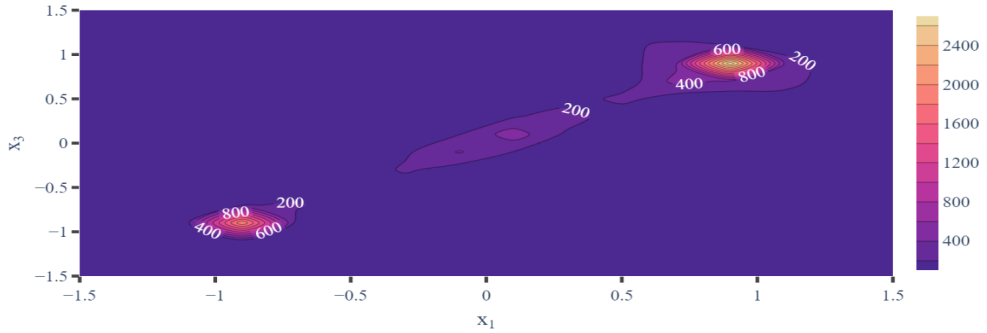
Figure 8: Poincaré map of $(x_1(t), x_2(t), x_3(t))$ at different values of fractional-order q



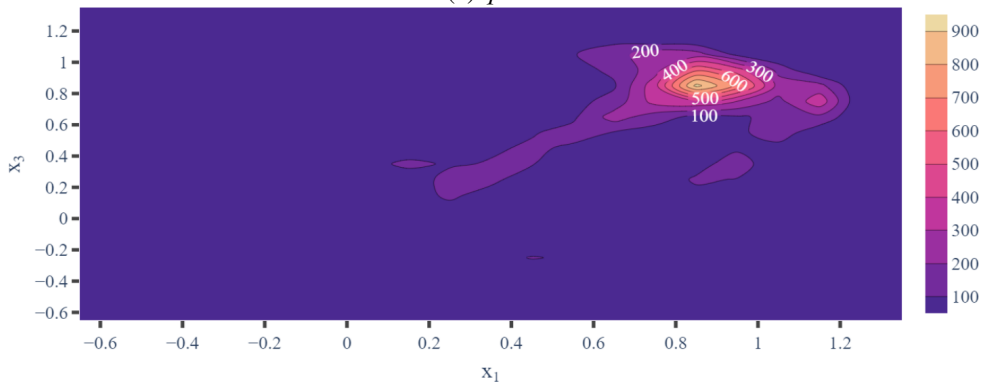
(a) $q = 1$



(b) $q = 0.99$



(c) $q = 1$



(d) $q = 0.99$

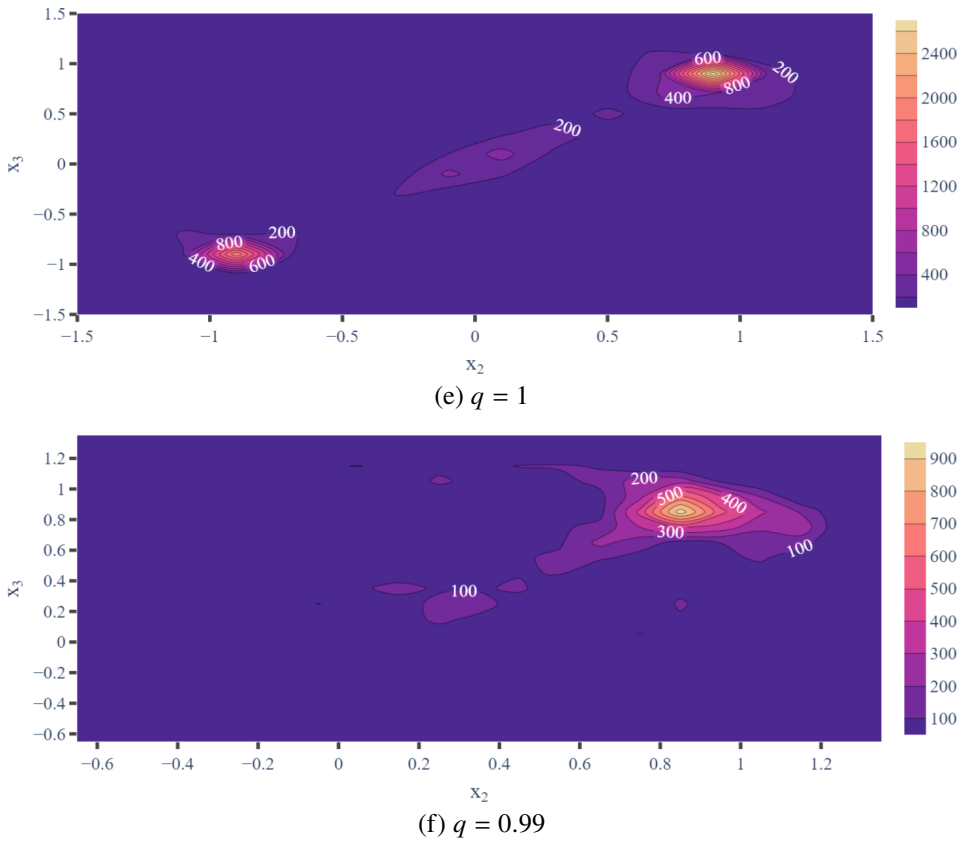
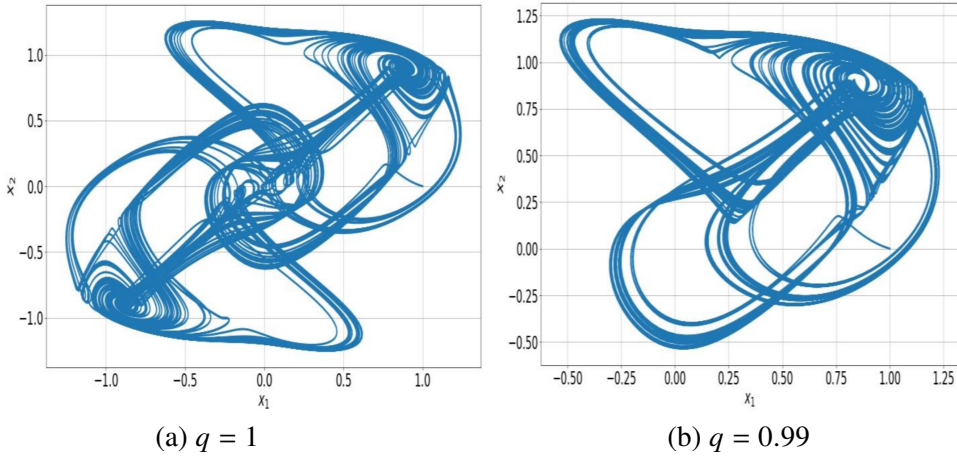


Figure 9: Contour plot of $(x_1(t), x_2(t), x_3(t))$ at different values of fractional-order q

3.1. Lyapunov exponents and Kaplan-Yorke dimension

The Lyapunov exponents (LEs) of a system are essential tools for determining whether the system is chaotic or non-chaotic. There are several approaches for computing the Lyapunov exponents, such as the Jacobian method [33], time-series based LEs calculation methods such as Wolf’s algorithm [34], and neural network algorithm [35], which are commonly used for computing Lyapunov exponents for fractional and integer-order systems. In this study, we used Wolf’s algorithm to calculate LEs. The Lyapunov exponents are calculated for system (4) with integer and fractional order $q = 1$ and $q = 0.99$ respectively. The values at integer order $q = 1$ are $(0.0896, 0, -0.9809)$ and at $q = 0.99$ the values are $(0.0520, -0.05266, -0.92940)$. Lyapunov exponents are presented in Fig. 10a–b. Figure 10a shows the Lyapunov exponents for $q = 1$ while Fig. 10b illustrates the Lyapunov exponents for $q = 0.99$. LEs at $q = 1$ and $q = 0.99$ show that the system (4) is chaotic because each of them consists of one positive, one negative and one which is almost zero.


 Figure 10: Lyapunov spectra at different values of fractional-order q

The Kaplan-Yorke dimension concerns the dimension of attractors by using Lyapunov exponents, which represent the complexity of an attractor is defined by the following:

$$D_{KY} = k + \frac{1}{|L_{k+1}|} \sum_{i=1}^k L_i, \quad (10)$$

where, L_i is Lyapunov exponents, k is the largest integer which satisfying the condition $\sum_{i=1}^k L_i \geq 0$ and $\sum_{i=1}^{k+1} L_i \leq 0$. The Kaplan-Yorke dimension of the system (4) is 2.08775 at fractional-order $q = 1$ and 1.93999 at fractional-order $q = 0.99$. The values of Kaplan-Yorke dimension shows that the complexity is decreasing with decreasing the fractional-order q .

4. Analog circuit simulation

In this section, the analog circuits are designed to verify the system (1) and (4). Firstly, we used the system (1) and converted it to circuital equations (9).

$$\begin{aligned} \dot{x}_1(t) &= -\frac{gx_1(t)}{R_1C_1} + \frac{hx_2(t)}{R_2C_1} - \frac{(x_2(t))^3}{R_3C_1}, \\ \dot{x}_2(t) &= -\frac{gx_2(t)}{R_4C_2} + \frac{hx_3(t)}{R_5C_2} - \frac{(x_3(t))^3}{R_6C_2}, \\ \dot{x}_3(t) &= -\frac{gx_3(t)}{R_7C_3} + \frac{hx_1(t)}{R_8C_3} - \frac{(x_1(t))^3}{R_9C_3}, \end{aligned} \quad (11)$$

where, $g = 0.3$, $h = 1.1$, R_i are resistors. The electronic circuit is made using fifteen resistors, three summing operational amplifiers and three inverting operational amplifiers, six multipliers and three capacitors. For oscilloscopic results, we select the resistors and capacitors values such as $R_1 = R_4 = R_7 = 333.333333333336 \Omega$, $R_2 = R_5 = R_8 = 90.909090909092 \Omega$, $R_3 = R_6 = R_9 = 125 \Omega$, $R_{10} = R_{11} = R_{12} = R_{13} = R_{14} = R_{15} = 100 \text{ k}\Omega$ and $C_1 = C_2 = C_3 = 1 \mu\text{F}$. The design circuit diagram of the system (9) is shown in Fig. 11 and its oscilloscopic diagram is in Fig. 13a–c.

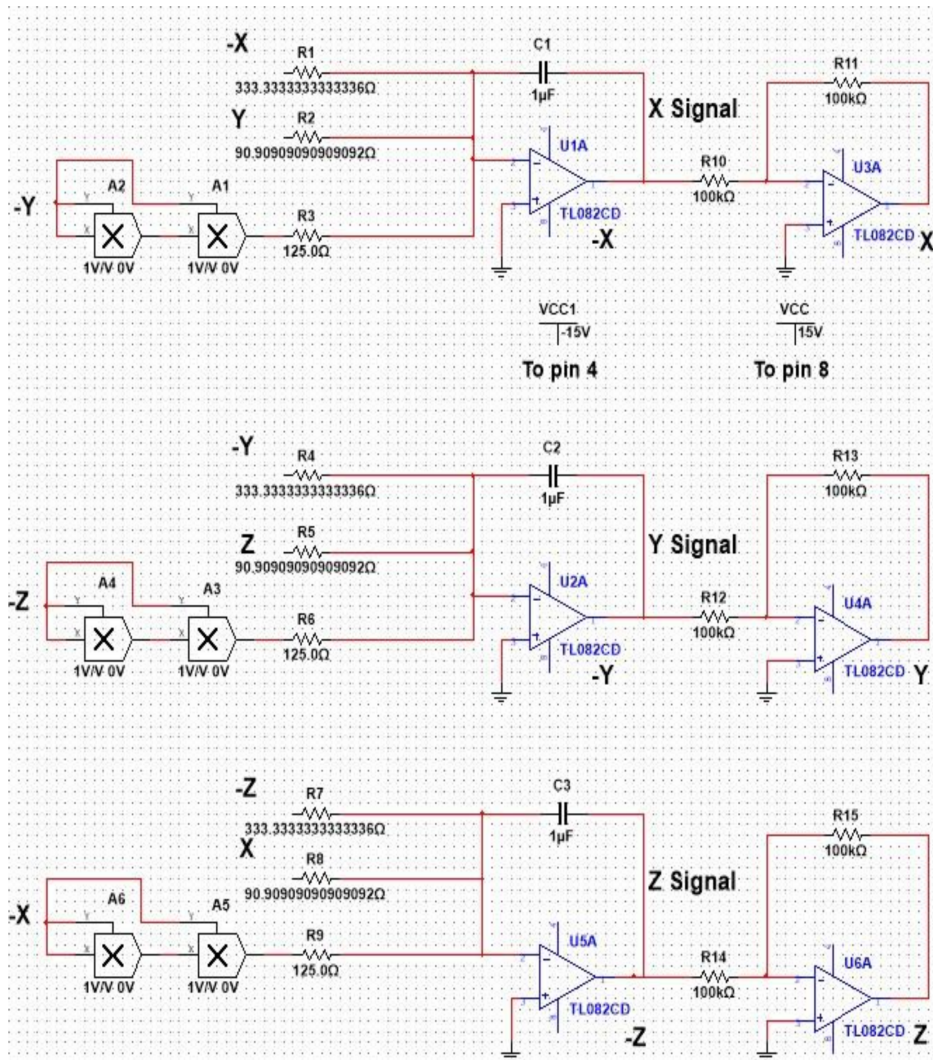


Figure 11: Schematic modal view of system (3) for $q = 1$ using *MultiSim*, (X signal represent $x_1(t)$, Y signal represents $x_2(t)$, Z signal represents $x_3(t)$)

For the fractional integrator we consider an approximate transfer function at $q = 0.99$, we can take the approximate formula defined as follows [36]:

$$\frac{1.137s^2 + 12640s + 130700}{s^3 + 11920s^2 + 132300s + 1369} \quad (12)$$

This transfer function can be realized with analog components. The realized fractional order integrator for $q = 0.99$ is given in Fig. 12 as fractional order

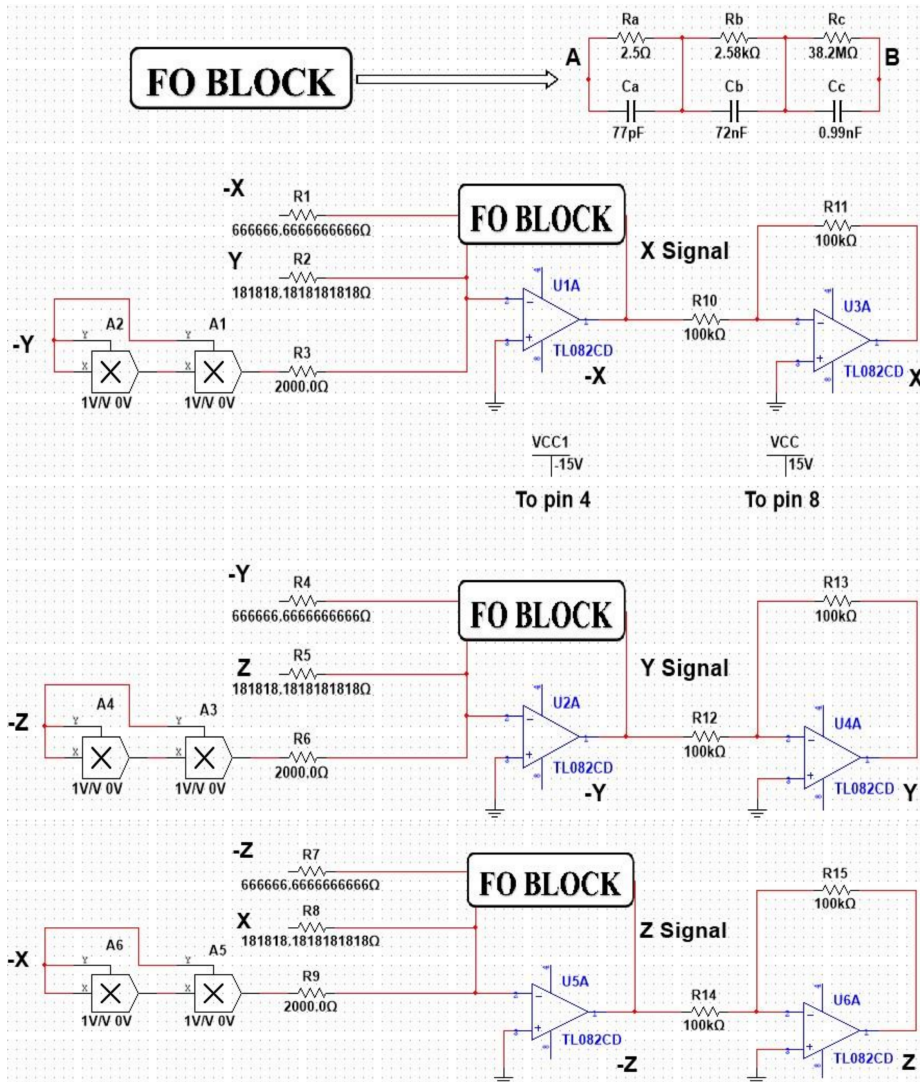
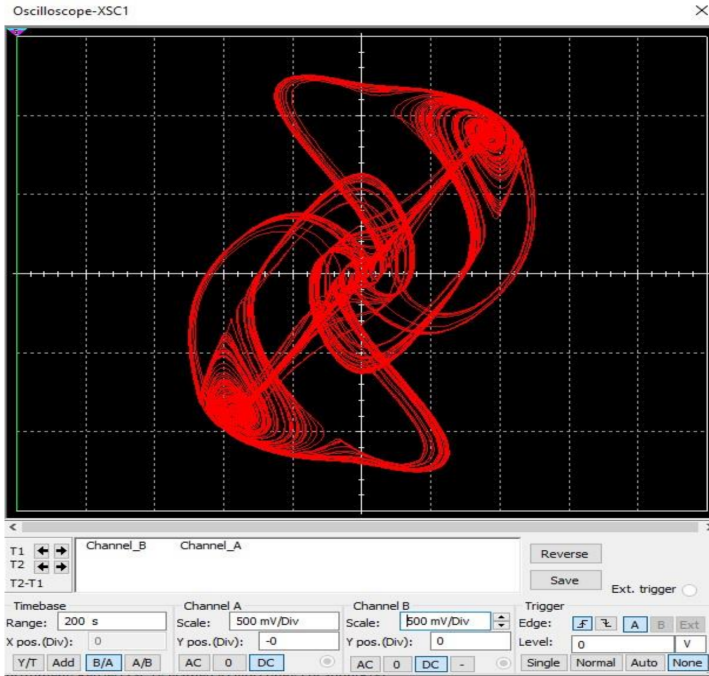
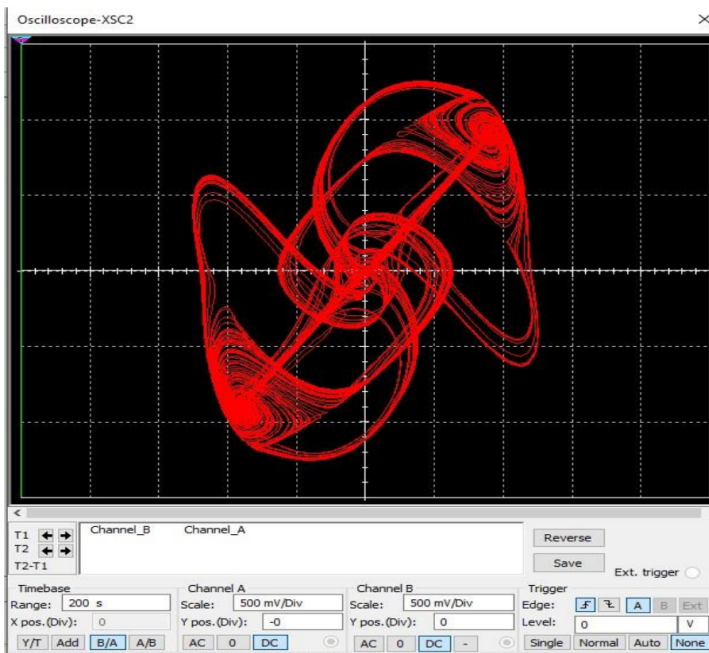


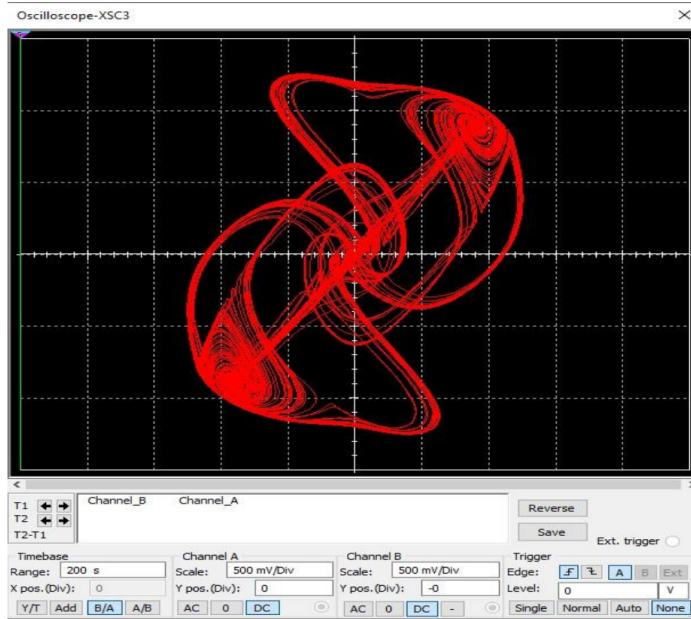
Figure 12: Schematic modal view of system (3) for $q = 0.99$ using *MultiSim*, (X signal represent $x_1(t)$, Y signal represents $x_2(t)$, Z signal represents $x_3(t)$)



(a) $(x_1(t), x_2(t))$ -plane



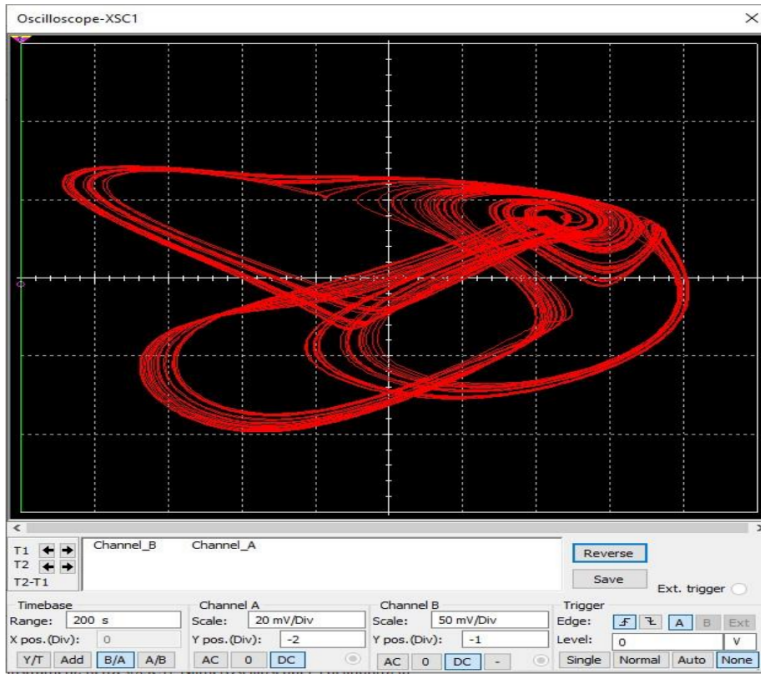
(b) $(x_1(t), x_3(t))$ -plane

(c) $(x_2(t), x_3(t))$ -planeFigure 13: Oscilloscopic phase plots of system (3) at $q = 1$

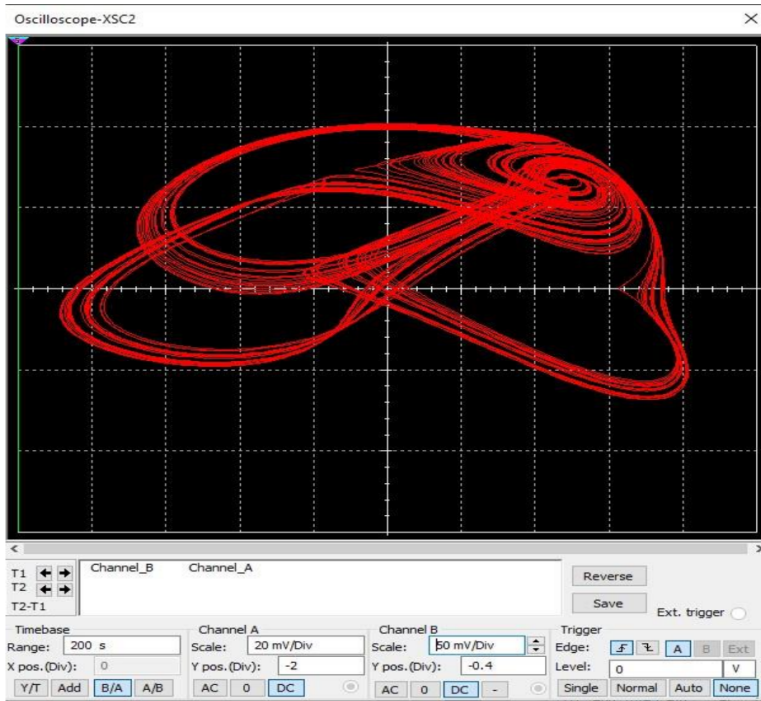
block (FO block) with normalized component values. The fractional chaotic system becomes

$$\begin{aligned}
 \dot{x}_1^{0.99}(t) &= -\frac{gx_1(t)}{R_1C_1} + \frac{hx_2(t)}{R_2C_1} - \frac{(x_2(t))^3}{R_3C_1}, \\
 \dot{x}_2^{0.99}(t) &= -\frac{gx_2(t)}{R_4C_2} + \frac{hx_3(t)}{R_5C_2} - \frac{(x_3(t))^3}{R_6C_2}, \\
 \dot{x}_3^{0.99}(t) &= -\frac{gx_3(t)}{R_7C_3} + \frac{hx_1(t)}{R_8C_3} - \frac{(x_1(t))^3}{R_9C_3},
 \end{aligned} \tag{13}$$

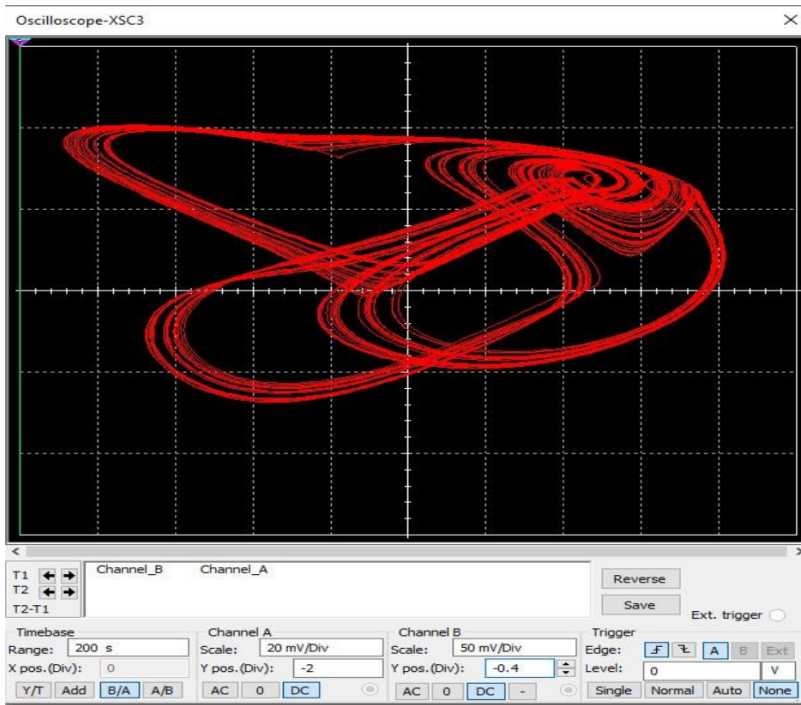
where $g = 0.3$, $h = 1.1$, R_i are resistors. The electronic circuit is made using twenty-four resistors, three summing operational amplifiers and three inverting operational amplifiers, six multipliers and six capacitors. For oscilloscopic results, we select the resistors and capacitors values such as $R_1 = R_4 = R_7 = 666666.6666 \Omega$, $R_2 = R_5 = R_8 = 181818.1818 \Omega$, $R_3 = R_6 = R_9 = 2 \text{ k}\Omega$, $R_{10} = R_{11} = R_{12} = R_{13} = R_{14} = R_{15} = 100 \text{ k}\Omega$ and $Ra = 2.5 \Omega$, $Rb = 2.58 \text{ k}\Omega$, $Rc = 38.2 \text{ M}\Omega$, $Ca = 77 \text{ pF}$, $Cb = 72 \text{ nF}$, $Cc = 0.99 \text{ nF}$. The design circuit diagram of the system (9) for $q = 0.99$ is shown in Fig. 12 and its oscilloscopic diagram is in Fig. 14a–c.



(a) $(x_1(t), x_2(t))$ -plane



(b) $(x_1(t), x_3(t))$ -plane

(c) $(x_2(t), x_3(t))$ -planeFigure 14: Oscilloscopic phase plots of system (3) at $q = 0.99$

5. Application on cryptography

5.1. Application on random number generators and cryptography

Chaotic systems play the role of the backbone in number generator and cryptography. System (4) was numerically simulated for a large amount of data after inserting the initial conditions and parameter values. The resulting float values were converted to 32-bit binary data, after which a single array was created for each variable. These arrays were passed through a NIST statistical suite for the conformation and randomness in system (4) in integer order. In Table 1, we see that all P-values are greater than 0.001, which is evidence of randomness. The encryption process is highly dependent on the chaotic systems that generate random numbers. With vast modern applications in the field of science and technology, the cryptography and cryptanalysis are the need of the day. This section presents the application of chaotic data in cryptography.

Table 1: The NIST-800-22 test results of system (4) at fractional-order $q = 1$

Statistical test	P-Value			Results
	$x_1(t)$	$x_2(t)$	$x_3(t)$	
Monobit Frequency Test	0.941377	0.863016	0.315330	Successful
Block Frequency Test	0.209916	0.263411	0.481346	Successful
Runs Test	0.805618	0.847513	0.273061	Successful
Longest Runs Ones 10000	0.931900	0.506463	0.039785	Successful
Binary Matrix Rank Test	0.963019	0.664131	0.219215	Successful
Spectral Test	0.619610	0.772767	0.782718	Successful
Non Over lapping Template Matching	0.345567	0.977761	0.367952	Successful
Over lapping Template Matching	0.226136	0.295813	0.370527	Successful
Maurer's Universal Statistic Test	0.989096	0.659299	0.189664	Successful
Linear Complexity Test	0.466789	0.617991	0.323151	Successful
Serial Test1	0.438362	0.410912	0.733211	Successful
Serial Test2	0.473857	0.330241	0.167331	Successful
Approximate Entropy Test	0.833791	0.635961	0.957118	Successful
Cumulative Sums Test	0.972525	0.788752	0.427273	Successful
Random Excursions Test at $x = -4$	0.898771	0.399058	0.549243	Successful
Random Excursions Variant Test $x = -9$	0.058351	0.569001	0.497321	Successful
Cumulative Sums Test Reverse	0.936982	0.736183	0.181514	Successful

5.2. Voice encryption

Voice encryption using chaotic data is performed using the XOR operation between the voice data and the data generated by our chaotic system. Figures 15a, b, and c show the original, encrypted, and decrypted images of the voice, respectively. The encrypted portion in Fig. 15b is completely fussy, indicating that decent and healthy encryption has various applications in the field of cryptography. The encryption is further tested with the magnitude spectrum of voice in Fig. 16, which suggests that the encrypted portion in Fig. 16a has high energy with respect to the frequency of voice data compared to the original and decrypted voices, as shown in Fig. 16a and Fig. 16c, respectively. Figure 17 shows the power spectrum density, which suggests that the variations are (dB/Hz) between the original and encrypted voices. Finally, the spectrogram of the voice is plotted in Fig. 18, which again shows good fussiness in Fig. 18b, which is the

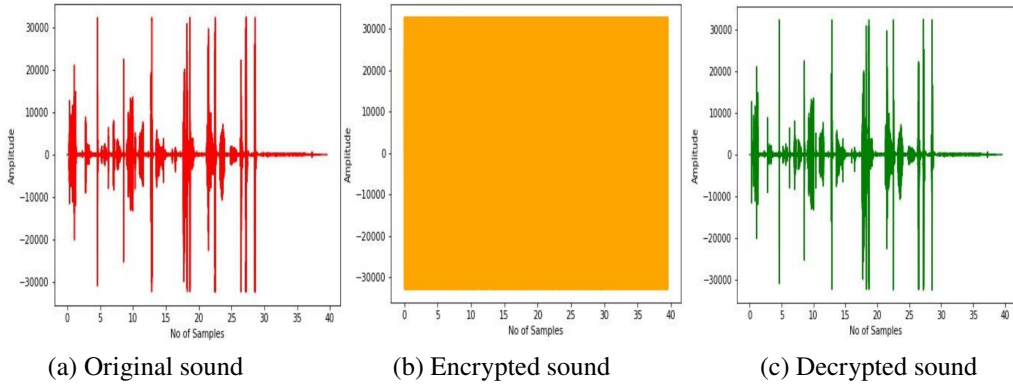


Figure 15: Sound data

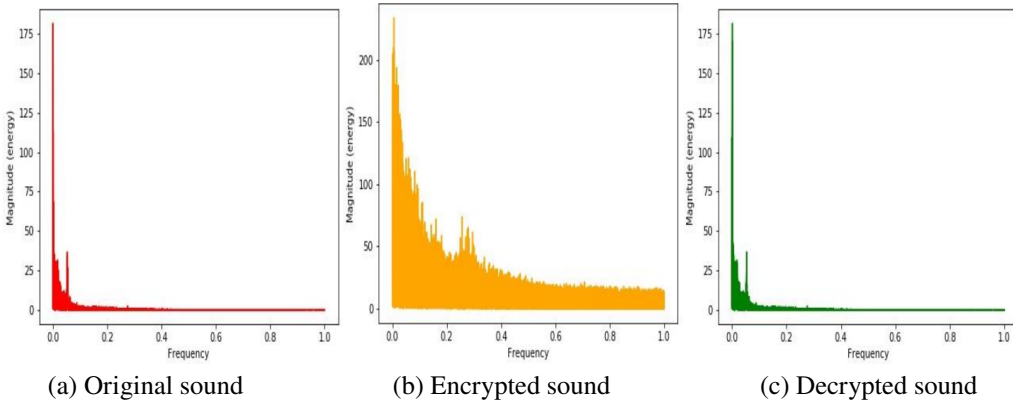


Figure 16: Magnitude spectrum of sound

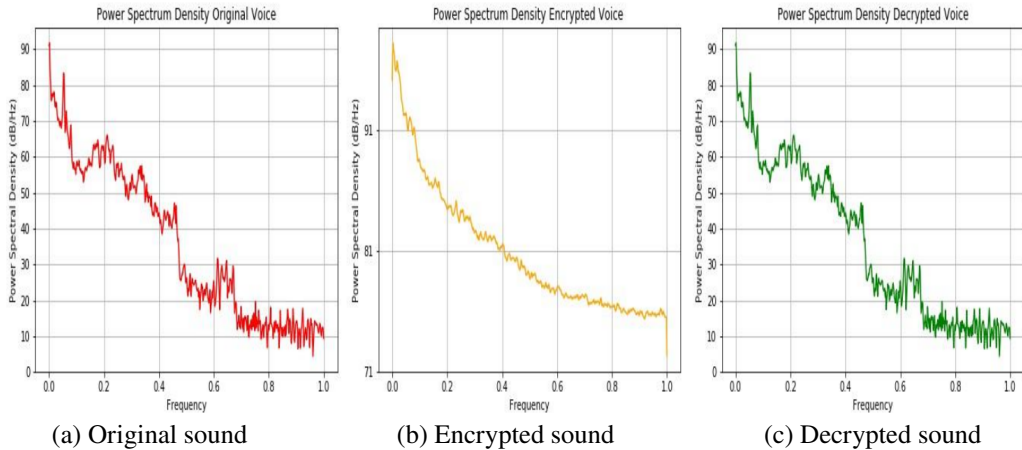


Figure 17: View of power spectrum density of sound data

spectrogram of the encrypted voice. The voice encryption *PYHTON* codes can be found in the repository of GitHub [37].

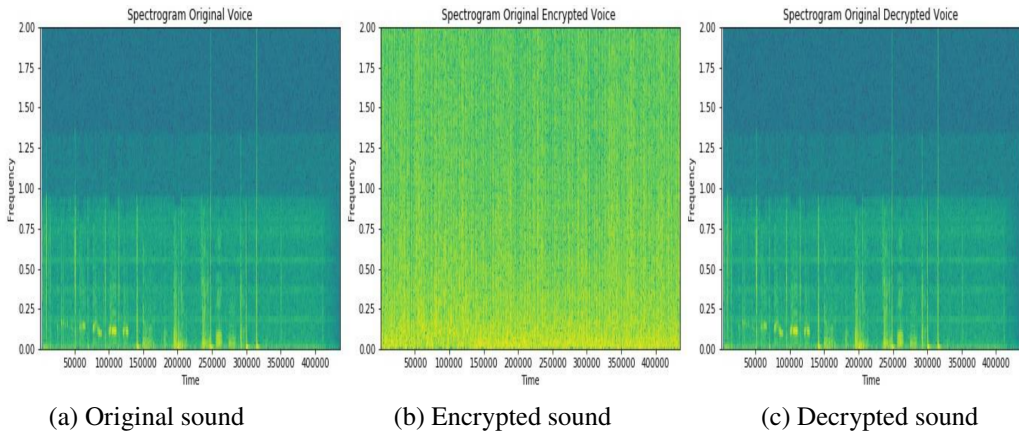


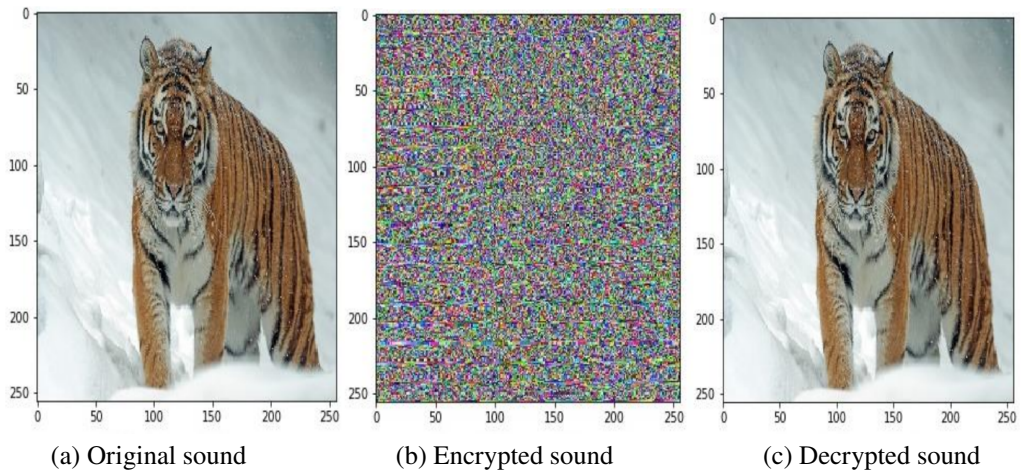
Figure 18: Spectrogram of sound data

5.3. Amalgamated image encryption

In this study, we developed a new algorithm for image encryption called amalgamated image encryption. The idea is to secure the image using two keys: (1) the three-dimensional al-flow chaotic data with initial conditions, and (2) the plain image. These two will behave like keys to successfully decrypt an image; failure to do so will result in an image that is very distorted and unrecognizable. To ensure this, we simulated both outcomes if the plain image key was successfully executed using the *PYHTON CV2* module, as presented in Figs. 20 and 23. Figure 20 (Tiger I) presents the encryption of plain image I with plain image II at fractional order $q = 0.99$, and similarly decrypted through plain image II with chaotic data at fractional order $q = 0.99$. The decrypted image is accurate as compared to the original image, and the image data are tested with security analysis, as mentioned in Table 1. Next, (Tiger II), we performed plain image I encryption using Plain Image II at fractional order $q = 0.99$, but decrypted through Plain Image III with chaotic data at fractional order $q = 0.99$. Because plain image III was not the accurate key, the outcome was considerably distorted and unrecognizable, as shown in Fig. 23. Both encrypted processes are plotted with histograms in Fig. 21, and Fig. 24 shows the distortion in the decrypted portion of the histogram in Fig. 24c when the image key is incorrect. Plain images are shown in Figs. 19a, b, and c. The algorithm and *PYHTON* codes of *Amalgamated Image Encryption* are available in GitHub [38].



Figure 19: Plain images utilized in encryption


 Figure 20: Tiger I (encryption of plain image I with plain pmage II at $q = 0.99$ and decrypted through plain image II with chaotic data at $q = 0.99$)

5.3.1. Security analysis of image encryption

Histogram

A uniform data distribution in encrypted images corresponds to good encryption, which can be examined by plotting histograms of plain original, encrypted, and decrypted images. To test our algorithm, Figs. 20 and 23 were investigated with a histogram. Figure 20 (Tiger I) shows that the original and decrypted image histograms are in good agreement, as the decryption is processed successfully. On the other hand, Fig. 23 (Tiger II) original and decrypted image histograms are not in good agreement, as the decryption is not processed successfully owing to

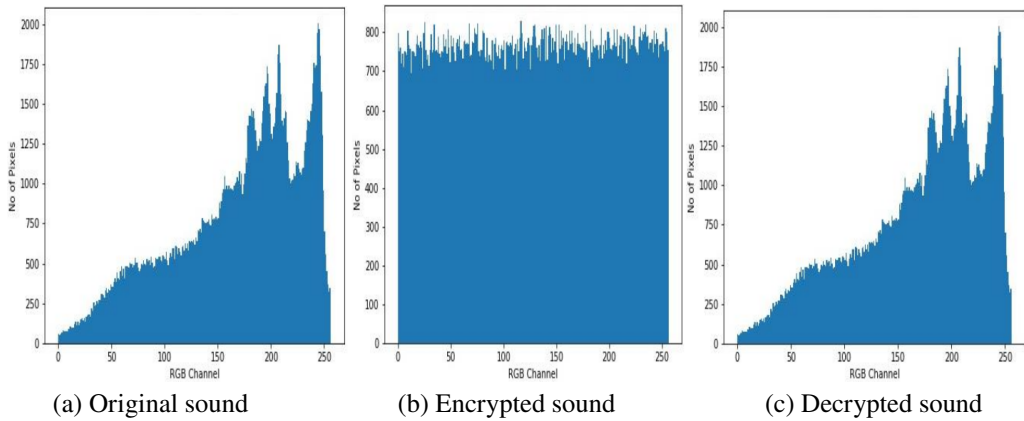


Figure 21: Histogram of Plain Image I original, encryption and decryption at $q = 0.99$ for Tiger I

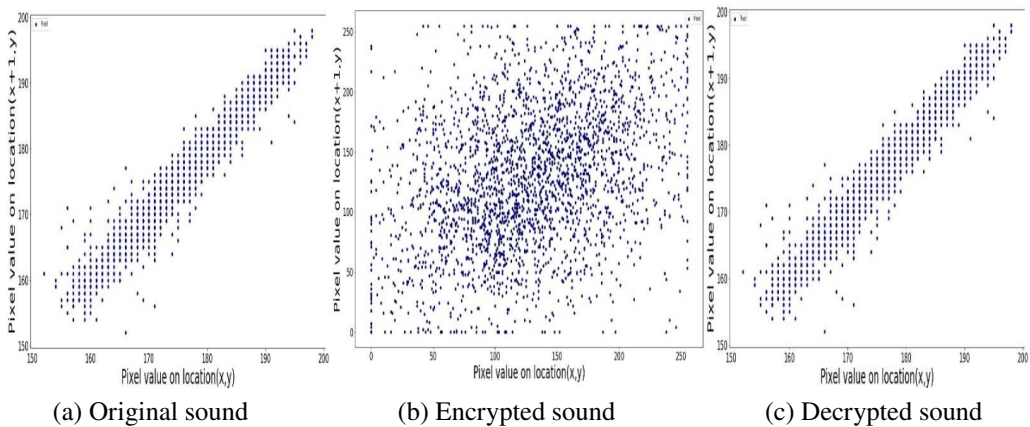


Figure 22: Pixel Correlation of Image I original, encryption and decryption at $q = 0.99$ for Tiger I

incorrect key utilization. In Figs. 20 and 23, the encrypted portion is completely distorted.

Correlation analysis

The pixel correlation in an image is assessed with the Correlation Analysis. In this regards the original, encrypted and decrypted images of Tiger I and Tiger II are analyzed in Table 2 with the formula below

$$\text{Correlation} = \sum_{j,k} \frac{(j - \eta_j) (k - \eta_k) p(j, k)}{\sigma_j \sigma_k} \tag{14}$$

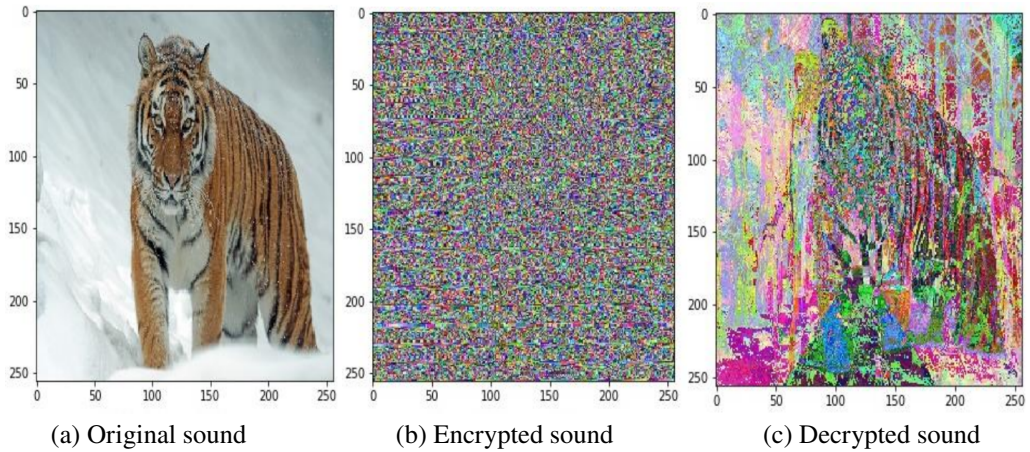


Figure 23: Tiger II (encryption of plain image I with plain image II at $q = 0.99$ and decrypted through plain image III with chaotic data at $q = 0.99$)

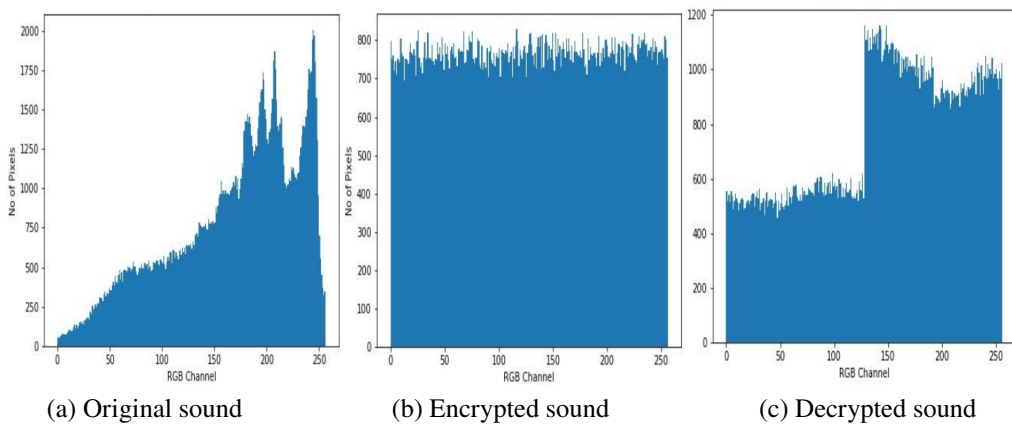


Figure 24: Histogram of plain image I original, encryption and decryption at $q = 0.99$ for Tiger II

The results show that the original and decrypted images are well correlated and are the same for Tiger I, whereas the original and decrypted images are well correlated but not the same for Tiger II, which means that the decryption is not successfully processed. The encrypted images are not well correlated, indicating good encryption. Further, the graphical correlation graphs are plotted in Figs. 22 and 25 for the Tiger I and Tiger II encryption and decryption processes. The correlation graph is the same for the original and decrypted images in Fig. 22 (Tiger I), whereas it is not the same for Fig. 25 (Tiger II). The encrypted portions

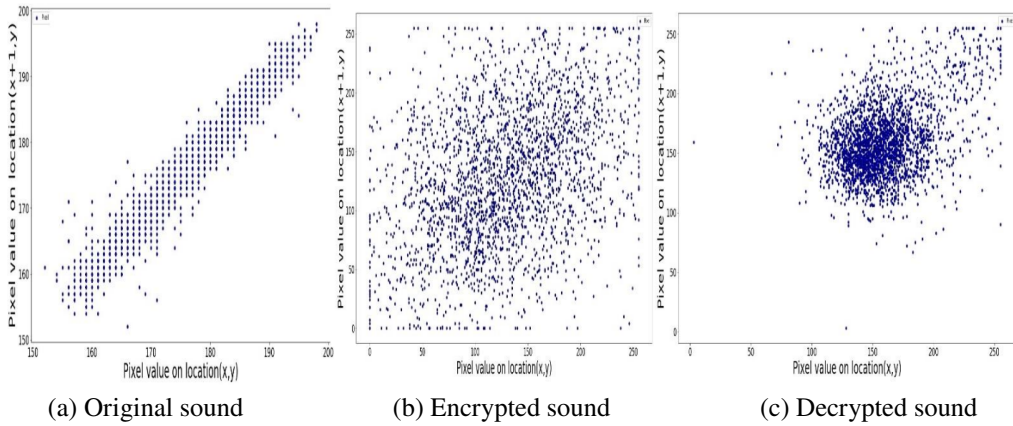


Figure 25: Pixel correlation of image I original, encryption and decryption at $q = 0.99$ for Tiger II

in Figs. 22b and 25b are completely haphazard, showing no pixel correlation with each other.

NPCR and UACI analysis

Number of Pixels Change Rate (NPCR) and Unified Average Changing Intensity (UACI) are two most important quantities to analyze the health of encryption. NPCR evaluates the percentage of different pixels between original and encrypted images. Mathematically it is calculated as

$$D(k, l) = \begin{cases} 0 & C(k, l) = C^*(k, l), \\ 1 & C(k, l) \neq C^*(k, l), \end{cases} \tag{15}$$

$$NPCR = \sum_{k=1}^M \sum_{l=1}^N \left[\frac{D(k, l)}{M \cdot N} \right] \times 100\%, \tag{16}$$

where, $C(k, l)$ and $C^*(k, l)$ characterize the pixel values of the two encrypted images.

The unified average changing intensity (UACI) indicates the average value of the changed pixel. It can be written as

$$UACI = \sum_{i=1}^M \sum_{j=1}^N \left[\frac{|C_1(i, j) - C_2(i, j)|}{255 \times M \times N} \right] \times 100\%. \tag{17}$$

The result for NPCR and UAIC are presented in Table 2.

Table 2: Results of PSNR, MSE NPCR, UAIC and correlation

Image	Dimension	MSE	PSNR	NPCR (%)	UAIC (%)	Correlation		
						Original image	Decrypted mage	Encrypted Image
Tiger I	256 × 256	0.00001	27.89761	99.60734	31.7564	0.90512	0.90512	0.33985
Tiger II	256 × 256	279710515.1722	27.89761	99.51375	31.7564	0.90512	0.58179	0.33985

Peak signal-to-noise ratio (PSNR)

Peak signal to noise ratio (PSNR) is calculated between the encrypted and original root mean squared valued and is defined as

$$PSNR = 10 \log_{10} \frac{(2^n - 1)^2}{MSE}. \quad (18)$$

For zero root mean square the PSNR has no importance

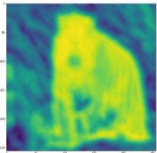
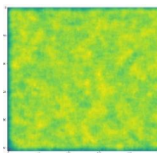
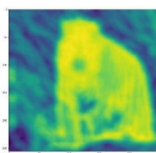
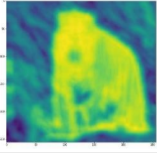
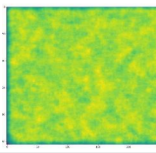
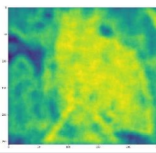
Entropy

Shannon's Information entropy of original, decrypted and encrypted images were calculated for respective images frames (i.e., red, green and blue) from formula below

$$H(s) = - \sum_{j=0}^{2^N-1} p(s_j) \log \left(\frac{1}{p(s_j)} \right). \quad (19)$$

The results of Tiger I and Tiger II are presented in Table 3. It is quite clear from the values that the Tiger I original and decrypted are in good agreement whereas

Table 3: Results of entropy

Image	Entropy			Entropy images			
		Original	Encrypted	Decrypted	Original	Encrypted	Decrypted
Tiger I	R	7.544348	7.775562	7.544348			
	G	7.649765	7.808275	7.649765			
	B	7.730009	7.762925	7.730009			
Tiger II	R	7.544348	7.775562	7.738319			
	G	7.649765	7.808275	7.848633			
	B	7.730009	7.762925	7.841358			

the Tiger II in not. Moreover, the average entropy for encrypted frames has more values than original and decrypted represents a secure encryption.

5.4. Video encryption

Figure 26 encloses the video original, encrypted and decrypted frames along with their histograms. As we know that the video consists of two basic data

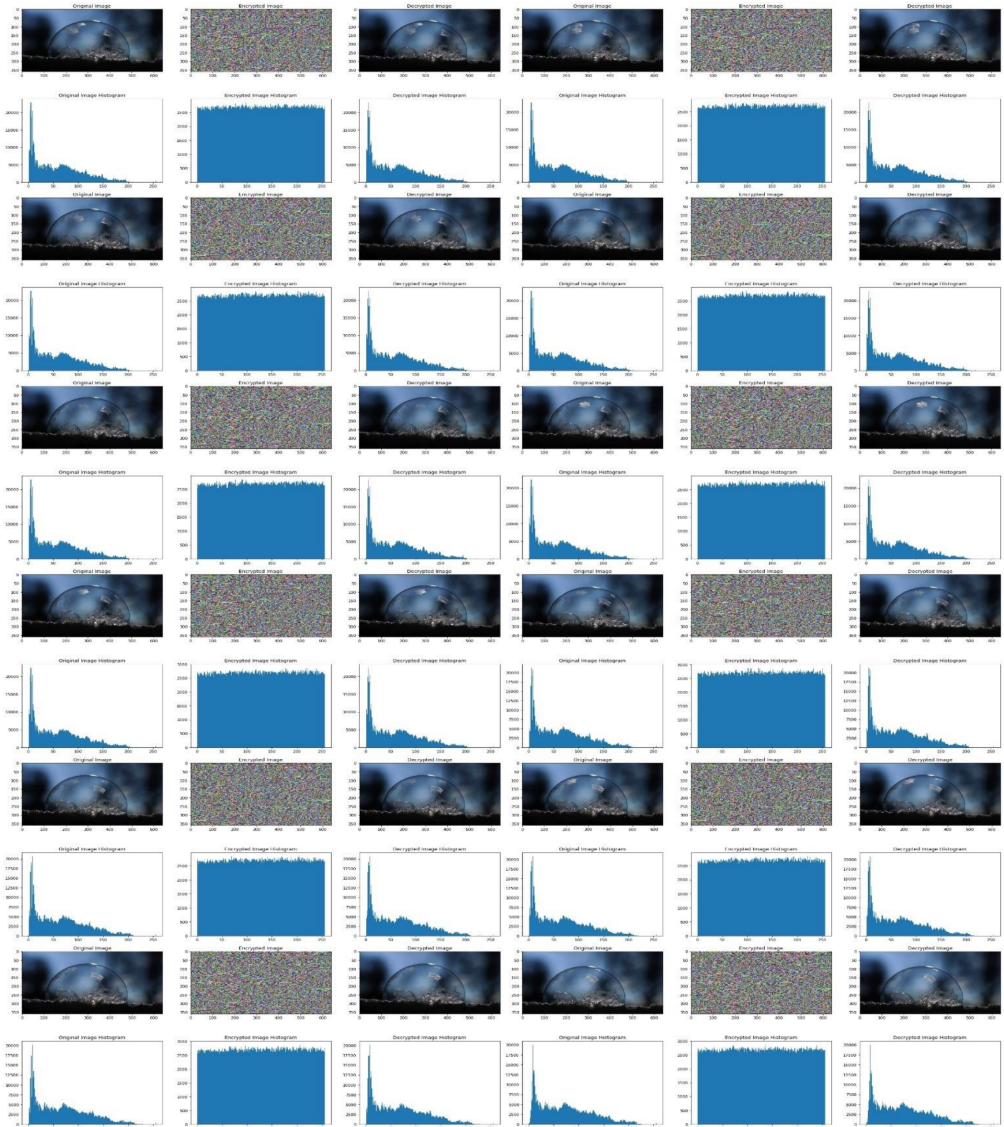


Figure 26: Frames of video original, encryption and decryption along with histograms at $q = 0.99$ for Soap Bubble (.mp4)

types, one is the voice and others is the frames of images that combine to give the video file. The video encryption here is done with *PYHTON* coding, which requires individual data types to encrypt separately and then merge them form a video. The *PYHTON* codes for video encryption are done with OpenCV module and are available in mentioned link [39].

6. Conclusion

In this paper, we present a three-dimensional fractional-order chaotic Thomas cyclically attractor and investigate its dynamic fractional behavior index. The idea behind this is to expand the chaotic regimes to find more complex systems that are sufficiently strong to encrypt our data for security. In this context, we qualitatively assessed Thomas system using phase portraits, Poincare maps, 2D contour plots, Lyapunov exponents, and NIST tests. Our investigation suggests that the integer model for Thomas' Cyclically attractor is more complex than fractional-order ones. This can be understood by observing phase portraits and 2D contour plots. Phase portraits give us the information that the system is symmetric for integer value $q = 1$, whereas for the non-integer $q = 0.99$, the symmetry is destroyed owing to sensitivity to initial conditions. Similarly, the 2D contour plot provides evidence that the system random number density is well established in two regions for $q = 1$, and the density of the data is only concentrated in one region for $q = 0.99$. Our investigation involves the analog circuit simulation of integer and fractional order systems, which agrees well with the numerically generated data. We used the transfer function to make a fractional integrator for the fractional-order circuit, while for the integer-order circuit; we used the simple circuit formation technique. The system nonlinearity is then applied to encrypt multimedia data like voice, images, and video to ensure our system's capability for a healthy encryption

- Investigated complexity in Thomas Cyclically Attractor for integer and fractional order system.
- Complexity evidence is investigated through 2D Contour plots and Phase Portraits.
- Thomas Cyclically integer and non-integer circuit simulation is presented in this work.
- Multimedia Cryptography is carried out; the encryption of voice, image and video is presented along with the security analysis of the image encrypted system.

Future work

1. So far, this study examined the Riemann-Liouville and proportional fractional derivative and its corresponding dynamic behavior, next we will examine Thomas Cyclically Symmetric Attractor with different fractional definitions and with different parameters.
2. In this paper the nonlinearity is utilized to do multimedia encryption, next our goal is to encrypt different document files like Pdf, Docx, etc.
3. Biometric encryption will apply to the multimedia and other document files for security purpose.
4. We will implement the Thomas Cyclically Symmetric Attractor on digital systems like FPGA.

References

- [1] H. WEIDENMÜLLER and G.E. MITCHELL: Random matrices and chaos in nuclear physics: Nuclear structure. *Reviews of Modern Physics*, **81**(2), (2009), 539. DOI: [10.1103/RevModPhys.81.539](https://doi.org/10.1103/RevModPhys.81.539).
- [2] C.W. HORTON and L.E. REICHL: *Statistical physics and chaos in fusion plasmas*. Wiley-Interscience, New York, 1984.
- [3] M. KYRIAZIS: Applications of chaos theory to the molecular biology of aging. *Experimental Gerontology*, **26**(6), (1991), 569–572. DOI: [10.1016/0531-5565\(91\)90074-v](https://doi.org/10.1016/0531-5565(91)90074-v).
- [4] D. GUEGAN: Chaos in economics and finance. *Annual Reviews in Control*, **33**(1), (2009), 89–93. DOI: [10.1016/j.arcontrol.2009.01.002](https://doi.org/10.1016/j.arcontrol.2009.01.002).
- [5] D.S. COFFEY: Self-organization, complexity and chaos: the new biology for medicine. *Nature Medicine*, **4**(8), (1998), 882–885. DOI: [10.1038/nm0898-882](https://doi.org/10.1038/nm0898-882).
- [6] J. LEE, C. LEE, and D.B. WILLIAMS: Secure communication using chaos. In Proceedings of the 1995 IEEE Global Telecommunications Conference, Singapore, (1995), Part 2, 1183–1187.
- [7] N.A. KHAN, T. HAMEED, and M.A. QURESHI: Emulate the chaotic flows of fractional jerk system to scramble the sound and image memo with circuit execution. *Physica Scripta*, **95**(6), (2020), 065217. DOI: [10.1088/1402-4896/ab8581](https://doi.org/10.1088/1402-4896/ab8581).

- [8] S. VAIDYANATHAN, A. SAMBAS, M. MAMAT, and M. SANJAYA: A new three-dimensional chaotic system with a hidden attractor, circuit design and application in wireless mobile robot. *Archives of Control Sciences*, **27**(4), (2017), 541–554. DOI: [10.1515/acsc-2017-0032](https://doi.org/10.1515/acsc-2017-0032).
- [9] S. VAIDYANATHAN, S. HE, and A. SAMBAS: A new multistable double-scroll 4-D hyperchaotic system with no equilibrium point, its bifurcation analysis, synchronization and circuit design. *Archives of Control Sciences*, **31**(1), (2021), 99–128. DOI: [10.24425/acs.2021.136882](https://doi.org/10.24425/acs.2021.136882).
- [10] E.N. LORENZ: Deterministic nonperiodic flow. *Journal of the Atmospheric Sciences*, **20**(2) (1963), 130–141. DOI: [10.1175/1520-0469\(1963\)020<0130:DNF>2.0.CO;2](https://doi.org/10.1175/1520-0469(1963)020<0130:DNF>2.0.CO;2).
- [11] T. WANG and X. WANG: A type of single scroll attractor chaos synchronization. *International Journal of Modern Physics B*, **24**(27), (2010), 5269–5283. DOI: [10.1142/S0217979210055500](https://doi.org/10.1142/S0217979210055500).
- [12] K. CHU, Z. ZHU, H. QIAN, and W. HUAGAN: Novel 3-scroll Chua's attractor with one saddle-focus and two stable node-foci. *Mathematical Problems in Engineering*, **2018** 917313. DOI: [10.1155/2018/8917313](https://doi.org/10.1155/2018/8917313).
- [13] Y. LI, X. XIA, Y. ZHENG, and Q. HONG: Composite one-to six-scroll hidden attractors in a memristor-based chaotic system and their circuit implementation. *Complexity*, **2020** 2020. DOI: [10.1155/2020/3259468](https://doi.org/10.1155/2020/3259468).
- [14] X. HU, C. LIU, L. LIU, J. NI, and S. LI: Multi-scroll hidden attractors in improved Sprott A system. *Nonlinear Dynamics*, **86**(3), (2016), 1725–1734. DOI: [10.1007/s11071-016-2989-5](https://doi.org/10.1007/s11071-016-2989-5).
- [15] B. VAN DER POL: A theory of the amplitude of free and forced triode vibrations. *Radio review*, **1** (1920), 701–710.
- [16] D.T. MARIS and D.A. GOUSSIS: The “hidden” dynamics of the Rössler attractor. *Physica D: Nonlinear Phenomena*, **1** (2015), 66–90. DOI: [10.1016/j.physd.2014.12.010](https://doi.org/10.1016/j.physd.2014.12.010).
- [17] T. MENACER, R. LOZI, and L.O. CHUA: Hidden bifurcations in the multispiral Chua attractor. *International Journal of Bifurcation and Chaos*, **26**(14), (2016), 1630039. DOI: [10.1142/S0218127416300391](https://doi.org/10.1142/S0218127416300391).
- [18] T. ZHOU, Y. TANG, and G. CHEN: Chen's attractor exists. *International Journal of Bifurcation and Chaos*, **14**(9), (2004), 3167–3177. DOI: [10.1142/S0218127404011296](https://doi.org/10.1142/S0218127404011296).

- [19] I. PEHLIVAN, E. KURT, Q. LAI, A. BASARAN, and M. KUTLU: A multiscroll chaotic attractor and its electronic circuit implementation. *Chaos. Theory and Applications*, **1**(1), (2019), 29–37.
- [20] E. TLELO-CUAUTLE, A. DE JESUS QUINTAS-VALLES, L.G. DE LA FRAGA, and J. DE JESUS RANGEL-MAGDALENO: VHDL descriptions for the FPGA implementation of PWL-function-based multi-scroll chaotic oscillators. *PLoS One*, **11**(12), (2016), e0168300. DOI: [10.1371/journal.pone.0168300](https://doi.org/10.1371/journal.pone.0168300).
- [21] M.I. RABINOVICH and A.L. FABRIKANT: Stochastic self-modulation of waves in nonequilibrium media. *Zhurnal Eksperimental'noi i Teoreticheskoi Fiziki*, **77** (1979), 617–629, (In Russian).
- [22] A.A. KILBAS, H.M. SRIVASTAVA, and J.J. TRUJILLO: *Theory and applications of fractional differential equations*. Elsevier, 2006.
- [23] N.A. KHAN, M.A. QURESHI, S. AKBAR, and A. ARA: From chaos to encryption using fractional order Lorenz-Stenflo model with flux-controlled feedback memristor. *Physica Scripta*, **98**(1), (2022), 014002. DOI: [10.1088/1402-4896/aca1e8](https://doi.org/10.1088/1402-4896/aca1e8).
- [24] T.T. HARTLEY, C.F. LORENZO, and H. KILLORY QAMMER: Chaos in a fractional order Chua's system. *IEEE Transactions on Circuits and Systems I: Fundamental Theory and Applications*, **42**(8), (1995), 485–490. DOI: [10.1109/81.404062](https://doi.org/10.1109/81.404062).
- [25] C. LI and G. CHEN: Chaos in the fractional order Chen system and its control. *Chaos, Solitons, and Fractals*, **22**(3), (2004), 549–554. DOI: [10.1016/j.chaos.2004.02.035](https://doi.org/10.1016/j.chaos.2004.02.035).
- [26] K. RAJAGOPAL, A. KARTHIKEYAN, and A.K. SRINIVASAN: FPGA implementation of novel fractional-order chaotic systems with two equilibriums and no equilibrium and its adaptive sliding mode synchronization. *Nonlinear Dynamics*, **87**(4), (2017), 2281–2304. DOI: [10.1007/s11071-016-3189-z](https://doi.org/10.1007/s11071-016-3189-z).
- [27] K. MOADDY, A. FREIHAT, M. AL-SMADI, E. ABUTEEN, and I. HASHIM: Numerical investigation for handling fractional-order Rabinovich–Fabrikant model using the multistep approach. *Soft Computing*, **22**(3), (2018), 773–782. DOI: [10.1007/s00500-016-2378-5](https://doi.org/10.1007/s00500-016-2378-5).
- [28] E. KASLIK and S. SIVASUNDARAM: Nonlinear dynamics and chaos in fractional-order neural networks. *Neural Networks*, **32** (2012), 245–256. DOI: [10.1016/j.neunet.2012.02.030](https://doi.org/10.1016/j.neunet.2012.02.030).

- [29] N.A. KHAN, M.A. QURESHI, T. HAMEED, S. AKBAR, and S. ULLAH: Behavioral effects of a four-wing attractor with circuit realization: a cryptographic perspective on immersion. *Communications in Theoretical Physics*, **72**(12), (2020), 125004. DOI: [10.1088/1572-9494/abb7d1](https://doi.org/10.1088/1572-9494/abb7d1).
- [30] N.A. KHAN, S. AKBAR, M.A. QURESHI, T. HAMEED, and N.A. KHAN: Qualitative study of the fractional order nonlinear chaotic model: electronic realization and secure data enhancement. *Journal of the Korean Physical Society*, **78**(2), (2021), 93–108. DOI: [10.1007/s40042-020-00017-7](https://doi.org/10.1007/s40042-020-00017-7).
- [31] H. ANTONIO, P.W.C PRASAD and A. ALSADOON: Implementation of cryptography in steganography for enhanced security. *Multimedia Tools and Applications*, **78**(23), (2019), 32721–32734. DOI: [10.1007/s11042-019-7559-7](https://doi.org/10.1007/s11042-019-7559-7).
- [32] R. THOMAS: Deterministic chaos seen in terms of feedback circuits: Analysis, synthesis, “labyrinth chaos”. *International Journal of Bifurcation and Chaos*, **9**(10), (1999), 1889–1905. DOI: [10.1142/S0218127499001383](https://doi.org/10.1142/S0218127499001383).
- [33] S. ELLNER, A.R. GALLANT, D. McCAFFREY and D. NYCHKA: Convergence rates and data requirements for Jacobian-based estimates of Lyapunov exponents from data. *Physics Letters A*, **153**(6-7), (1991), 357–363. DOI: [10.1016/0375-9601\(91\)90958-B](https://doi.org/10.1016/0375-9601(91)90958-B).
- [34] A. WOLF, J.B. SWIFT, H.L. SWINNEY, and J.A. VASTANO: Determining Lyapunov exponents from a time series. *Physica D: Nonlinear Phenomena*, **16**(3), (1985), 285–317. DOI: [10.1016/0167-2789\(85\)90011-9](https://doi.org/10.1016/0167-2789(85)90011-9).
- [35] A. MAUS and J. SPROTT: Evaluating Lyapunov exponent spectra with neural networks. *Chaos, Solitons & Fractals*, **51** (2013), 13–21. DOI: [10.1016/j.chaos.2013.03.001](https://doi.org/10.1016/j.chaos.2013.03.001).
- [36] B. ARICIOĞLU: RNG and circuit implementation of a fractional order chaotic attractor based on two degrees of freedom nonlinear system. *Analog Integrated Circuits and Signal Processing*, **112**(1), (2022), 49–63. DOI: [10.1007/s10470-022-02040-z](https://doi.org/10.1007/s10470-022-02040-z).
- [37] M.A. QURESHI: Encryption-python-codes: release of voice and image encryption in Python. *Zenodo*, (2020). DOI: [10.5281/zenodo.3693098](https://doi.org/10.5281/zenodo.3693098).
- [38] M.A. QURESHI: Amalgamated image encryption. Circuit realization for Lorenz-Stenflo chaotic system. *Zenodo*, (2022). DOI: [10.5281/zenodo.7046557](https://doi.org/10.5281/zenodo.7046557).
- [39] M.A. QURESHI: Release of video encryption in Python. *Zenodo*, DOI: [10.5281/zenodo.5499881](https://doi.org/10.5281/zenodo.5499881).